





## Probing many-body localization on a noisy quantum computer

D. Zhu <sup>1,2,\*</sup> S. Johri,<sup>3,†</sup> N. H. Nguyen <sup>1</sup> C. Huerta Alderete <sup>1,4</sup> K. A. Landsman <sup>1,2</sup>  
N. M. Linke,<sup>1</sup> C. Monroe,<sup>1,2</sup> and A. Y. Matsuura<sup>3</sup>

<sup>1</sup>*Joint Quantum Institute and Department of Physics, University of Maryland, College Park, Maryland 20742, USA*

<sup>2</sup>*Center for Quantum Information and Computer Science, University of Maryland, College Park, Maryland 20742, USA*

<sup>3</sup>*Intel Labs, Intel Corporation, Hillsboro, Oregon 97124, USA*

<sup>4</sup>*Instituto Nacional de Astrofísica, Óptica y Electrónica, Sta. Ma. Tonantzintla, Puebla 72840, Mexico*



(Received 7 July 2020; revised 18 January 2021; accepted 22 February 2021; published 15 March 2021)

A disordered quantum system of interacting particles exhibits localized behavior when the disorder is large compared to the interaction strength. Studying this phenomenon on a quantum computer with no, or limited, error correction is challenging because even weak coupling to a thermal environment destroys most signatures of localization. Fortunately, spectral functions of local operators are known to contain features that can survive the presence of noise. In these spectra, discrete peaks and a soft gap at low frequencies compared to the thermal phase indicate localization. Here, we present the computation of spectral functions on a trapped-ion quantum computer for a one-dimensional Heisenberg model with disorder. Further, we design an error-mitigation technique which is effective at removing the noise from the measurement allowing clear signatures of localization to emerge as the disorder increases. Thus, we show that spectral functions can serve as a robust and scalable diagnostic of many-body localization on current and future generations of quantum computers.

DOI: [10.1103/PhysRevA.103.032606](https://doi.org/10.1103/PhysRevA.103.032606)

Many-body localization (MBL) is a phenomenon which emerges in quantum systems with both interactions and disorder. At large values of disorder, a many-body system can fail to thermalize even at high temperatures causing it to exhibit properties like long-term memory retention, logarithmic entanglement growth in time, and area-law entanglement scaling [1,2]. The many-body localization-delocalization transition, which occurs at a critical disorder strength, is a dynamical phase transition. This necessitates the study of excited states, rather than just the ground state of the system. The study of this phenomenon in spin systems via full diagonalization exhausts classical computational power for a system of about 20 spins [3]. Specialized approximate schemes such as tensor network methods can in principle handle larger system sizes but tend to only work well for short-range interacting systems in one dimension away from the phase transition [4,5]. Many open questions still abound regarding the effects of symmetry, topology, dimensionality, long-range interactions, thermal inclusions, and the universality class of the disorder, especially near the phase transition. Better simulations of this phenomenon would also lead to a deeper understanding of fundamental concepts in quantum thermodynamics such as the eigenstate thermalization hypothesis. Thus, the study of a many-body localized system has been proposed as a benchmark for showing the utility of near-term quantum computers that are capable of noisy but classically unapproachable computations [6].

Experimental efforts to probe MBL include quantum simulators consisting of thousands of cold atoms [7–12] and a Hamiltonian whose disorder arises from the superposition of lattice potentials with incommensurate wavelengths. Another set of leading examples are experiments on trapped ions with tens of spins, which investigate the role of disorder in long-range Ising chains [13,14]. Finally, up to three interacting photons in an array of transmons with random on-site energies have been studied [15,16]. A limitation of all of these experiments is that they are specialized to a particular class of Hamiltonians that are native to the system and therefore cannot address many open questions about MBL. The only simulation of MBL on a quantum computer operated in a universal fashion was limited to a two-spin system realized with transmon qubits [17]. Additionally, the energy statistics and entanglement entropy studied in [15,16] take exponentially longer to measure as the number of interacting particles increases. Another problem arises from the noise in near-term quantum computers, which manifests itself as a thermal bath coupled to the system. Since diagnostics like level statistics and entanglement growth have been shown to revert to thermal behavior on even weak coupling to a thermal bath [18], they are particularly unsuitable for the study of localization on such near-term devices.

Here, we introduce a technique for studying MBL on universal quantum computers by measuring the spectral functions of local operators. These carry signatures of localization that are known to survive coupling to a thermal bath as long as it is weaker than the characteristic energy scales of the model [18]. We measure spectra for the Heisenberg model with disordered magnetic fields along two directions implemented by three qubits on an ion trap quantum computer. In the many-body

\*daiwei@terpmail.umd.edu

†Present affiliation: IonQ Inc., 4505 Campus Drive, College Park, Maryland 20740.

localized phase, the spectral functions exhibit a discrete nature, and after averaging over disorder, display a suppression of amplitude or “soft gap” at low frequencies, compared to the thermalized phase. In addition to the natural robustness to noise of our chosen observables, we also design an error mitigation scheme specific to the study of disorder-averaged spectral functions.

For a given Hamiltonian  $H$  with eigenstates  $|\phi_m\rangle$  and corresponding eigenenergies  $E_m$ , the spectral function of an operator  $\hat{a}$  is defined as

$$A(\omega) = \sum_{l,k} |\langle \phi_l | \hat{a} | \phi_k \rangle| \delta_{\omega, E_k - E_l}, \quad (1)$$

where  $\delta$  is the Kronecker delta, and  $\omega$  is the frequency in units of energy/ $\hbar$ . We take  $\hbar = 1$  throughout this study.

For our study, we choose the one-dimensional Heisenberg model with random fields along two axes which for  $n$  spins has the Hamiltonian,

$$H = J \sum_{i=1}^{n-1} \hat{\sigma}_i^x \hat{\sigma}_{i+1}^x + w \left( \sum_{i=1}^n h_i^x \hat{\sigma}_i^x + \sum_{i=1}^n h_i^z \hat{\sigma}_i^z \right). \quad (2)$$

Here,  $\hat{\sigma}_i = (\hat{\sigma}_i^x, \hat{\sigma}_i^y, \hat{\sigma}_i^z)$  are the Pauli operators.  $J$  determines the nearest neighbor coupling strength.  $w$  is the a coefficient that determines the global strength of the external fields. The disorder in the model comes from the fields  $h_i^x$  and  $h_i^z$ , which are random variables chosen from a uniform probability distribution between  $-1$  and  $1$ . In the limit  $w/J \rightarrow 0$ , the system is in the thermalized phase and for  $w/J \rightarrow \infty$ , it is in the localized phase. This model is known to have a phase transition at  $w/J \sim 6$  [19]. We set  $w = 1$ .

For a local operator  $\hat{a}$  such as a single spin Pauli operator, the spectral function  $A(\omega)$  for  $n$  spins at  $J = 0$  will consist of  $2n$   $\delta$  functions at  $\pm 2w\sqrt{h_i^x{}^2 + h_i^z{}^2}$ . The average spacing between the peaks is  $\sim w/n$ . For  $0 < J \ll w$ , each peak of the noninteracting spectrum will split into a cluster of  $\delta$  functions with a hierarchy of energy gaps [18,20]. The full width of the cluster is  $J \exp(-1/\xi)$ , where  $\xi$  is the localization length which is an increasing function of  $J/w$  (see Appendix C). When the system is coupled to a thermal bath, the spectral lines broaden and the discrete structure gradually vanishes as the coupling strength increases. It disappears only when the coupling becomes comparable to  $J$ . In contrast, in the thermal phase,  $A(\omega)$  is expected to become an increasingly smooth function of energy as  $n$  increases. Here we construct the probability distribution of the widths of these clusters from the linewidths  $\Gamma$  of the peaks in the spectrum.

After averaging over spin locations and disorder realizations, the ratio of the averaged spectrum of the localized phase to that of the thermalized phase should go to zero as  $\omega \rightarrow 0$  [20]. This implies that in the localized phase, local operators are less likely to connect nearby energy eigenstates, instead mixing them and giving rise to level repulsion. The width of the resulting spectral soft gap is a function of  $w$  and remains finite in the thermodynamic limit. In contrast, in the thermalized phase, the spectral function decays as  $\omega$  increases for  $\omega < J$  [1].

As we now show, the spectral functions can be approximated on a quantum computer by Hamiltonian time evolution, followed by measurement of the expectation value of the local

operator and a Fourier transform of the resulting time series data. At  $t = 0$ , let the system be in the state,

$$|\Psi(t=0)\rangle = \sum_k c_k |\phi_k\rangle, \quad (3)$$

where  $|k\rangle$  are the eigenstates of the system. The expectation value of operator  $\hat{a}$  at time  $t$  is

$$\langle \hat{a}(t) \rangle = \sum_{k,l} c_k c_l^* a_{kl} e^{-i(E_k - E_l)t}, \quad (4)$$

where  $a_{kl} = \langle \phi_l | \hat{a} | \phi_k \rangle$ . The absolute value of the Fourier transform of the above expression gives

$$\mathcal{F}\{|\langle \hat{a} \rangle|\} = \sum_{k,l} |c_k c_l^* a_{kl}| \delta_{\omega, E_k - E_l}. \quad (5)$$

Note the similarity to the spectrum of  $\hat{a}$  from Eq. (1), especially when the initial state [Eq. (4)] is spread over the eigenstates of the system. In the experiment we use  $\hat{a} = \hat{\sigma}_i^z$ , and initialize the qubits in the  $|+\rangle$  state, which is an equal superposition of the two eigenstates of  $\hat{a}$ . We measure in the  $z$  basis at the end, in order to extract the spectral function corresponding to  $\hat{\sigma}_i^z$  for qubit  $i$ . When discussing the experimental measurement of  $\bar{A}(\omega)$ , we are referring to the expression in Eq. (5) after disorder averaging.

The experiment is conducted on a re-configurable system with up to nine qubits, where each qubit is realized by the hyperfine-split ground states of a  $^{171}\text{Yb}^+$  ion. Here we use  $n = 3$  qubits. A universal set of quantum gates consisting of arbitrary single-qubit rotations and XX(Ising) gates between any pair of qubits can be applied (see the Appendix for details). The study of disordered systems requires averaging over many disorder realizations. We run the experiment for different values of the coupling strength:  $J = 0.1$ ,  $J = 0.3$ , and  $J = 0.7$ , using 24 circuits each to sample instances of disorder. The choice of sample size for each coupling strength can, according to simulation, guarantee low enough statistical uncertainty. The circuits are generated beforehand and fed to the experiment control computer in batches. As long as the ions stay trapped, the system automatically executes the circuits sequentially. The quantum circuit corresponding to the time evolution under  $H$  is shown in Fig. 1. The Hamiltonian evolution cannot be implemented exactly on digital quantum computers (with finite number of gates). We use Trotterization to decompose it into one- and two-qubit gates [Fig. 1(b)]. The two-qubit interaction is exactly captured by the unitary  $U$  since  $XX$ ,  $YY$ , and  $ZZ$  terms commute with each other. Each Trotter step achieves the following unitary:

$$\hat{U}_H = \prod_{k=1}^n (e^{-ih_{x,k} \hat{\sigma}_k^x \delta} e^{-ih_{x,k} \hat{\sigma}_k^x \delta}) \times \prod_{k=1}^{n-1} (e^{-iJ \hat{\sigma}_k^z \hat{\sigma}_{k+1}^z \delta} e^{-iJ \hat{\sigma}_k^y \hat{\sigma}_{k+1}^y \delta} e^{-iJ \hat{\sigma}_k^x \hat{\sigma}_{k+1}^x \delta}). \quad (6)$$

The total evolution time is given by  $t = m\delta$ . It is straightforward to extend the circuit to an arbitrary number of qubits.

The time evolution is sampled at 10 different equally spaced intervals between  $0 < t \leq 10$ . The expectation value of  $\hat{\sigma}_z$  at  $t = 0$  is trivially known to be zero. We use a constant

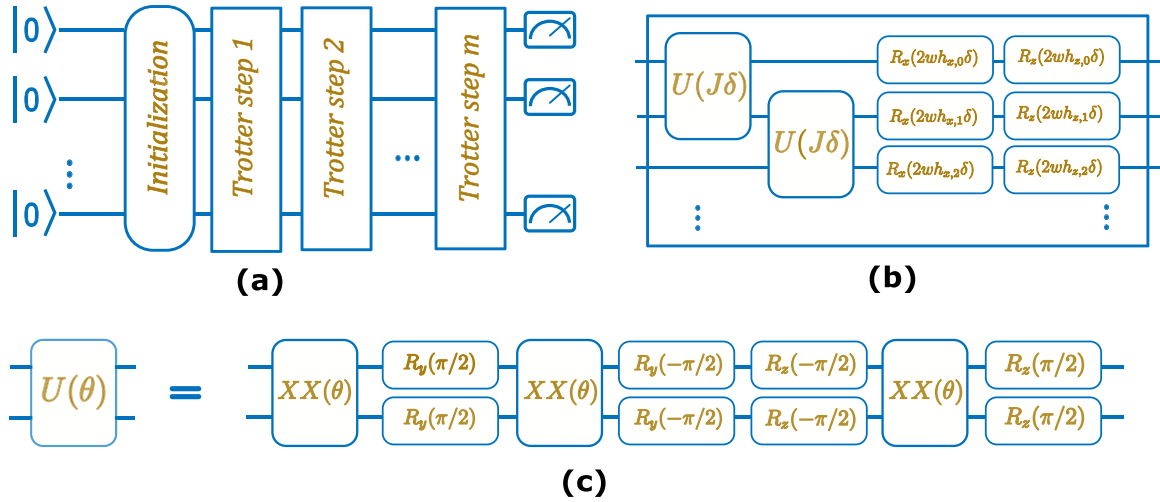


FIG. 1. The circuit used to simulate time evolution under the Heisenberg model Hamiltonian. (a) After the qubits are prepared into the desired initial state,  $m = 6$  Trotter steps are used to evolve the system to time  $t$ . All qubits are then measured in the  $z$  basis. (b) Each Trotter step consists of several one- and two-qubit gates, as described by Eq. (6). The single-body interactions are implemented as rotations about the  $X$  or  $Z$  axis ( $R_x$  and  $R_z$  gates). (c) The two-body interactions  $\hat{U}(J\delta)$  are implemented as three  $XX$  (Ising) gates sandwiched between single-qubit rotations. This segment of the circuit is equivalent to a sequential application of  $XX$ ,  $YY$ ,  $ZZ$  gates, which describes evolution under the Heisenberg interaction exactly.

number  $m = 6$  Trotter steps for each sample time making the Trotter angle  $\delta = t/6$ . This is in contrast to the more widely used method of Trotterization where  $\delta$  stays fixed and the number of Trotter steps increases with time. Since the number of Trotter steps is constant no matter the simulation time, the magnitude of experimental error is the same in every circuit [21]. We will see that this becomes critical to the error mitigation technique we introduce below.

Each circuit is measured 2400 times to sufficiently reduce the statistical error. We initialize all qubits into  $|+\rangle$  states with Hadamard gates. Because the  $|+\rangle^{\otimes n}$  state is an eigenstate of the  $\hat{U}$  operator, we can skip the application of the first set of  $\hat{U}$  gates on all qubits. Each circuit thus consists of 30 two-qubit gates and 116 single-qubit gates. We run a total of 792 circuits to obtain the data in this paper.

A discrete Fourier transform is then applied to the time series for each instance to obtain the spectrum. In the thermodynamic limit,  $J = 0.1$  lies in the localized phase,  $J = 0.7$  in the thermalized and  $J = 0.3$  near the phase transition. For a small system, there is no sharp phase transition but we expect to see a change from thermalized to localized behavior as we lower the value of  $J$ .

Figure 2 shows several instances of the measured spectrum for  $\hat{\sigma}_i^z$ . The spectrum is symmetric about  $\omega = 0$ . We note that the experimental data is significantly damped compared to the simulation. The figure also shows the necessity of averaging over several realizations in the study of disordered systems since the behavior of the system in the thermodynamic limit cannot be determined from the behavior of a finite-size individual disorder realization.

We next average the spectral functions over lattice sites and disorder configurations. The results are shown in Figs. 3(a)–3(c). The value at  $\omega = 0$  arises from the diagonal elements and is related to the equilibrium value of the observable at infinite temperature, whereas the behavior at  $\omega > 0$  gives the dynamical response of the system. The simulation curves

show that the value of the spectral function at low frequencies drops as  $J$  decreases. Simulation results for a larger system size show similar behavior (Appendix B). While the experimental data follow the trend of the simulation for each value of  $J$ , the error obscures the difference between the spectra at different values of  $J$ . To address this, we now introduce an error mitigation technique.

It has been shown that the error in the mean value of an observable measured after the application of a set of random

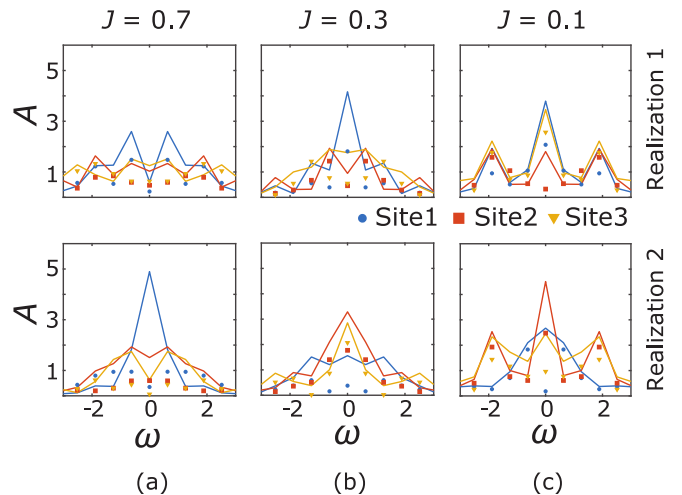


FIG. 2. The spectrum of  $\hat{\sigma}_i^z$  at different values of  $J$  (with  $w = 1$ ) for a three-site system for two sample disorder realizations (top and bottom). Each panel shows both simulation (curves) and experimental (symbols) results. The different colors are for the different sites. The lack of distinguishing characteristics between the spectra at different values of  $J$  for individual samples shows the necessity of averaging over several disorder realizations. With 2400 repetitions, the statistical error bars are smaller than the plot markers.

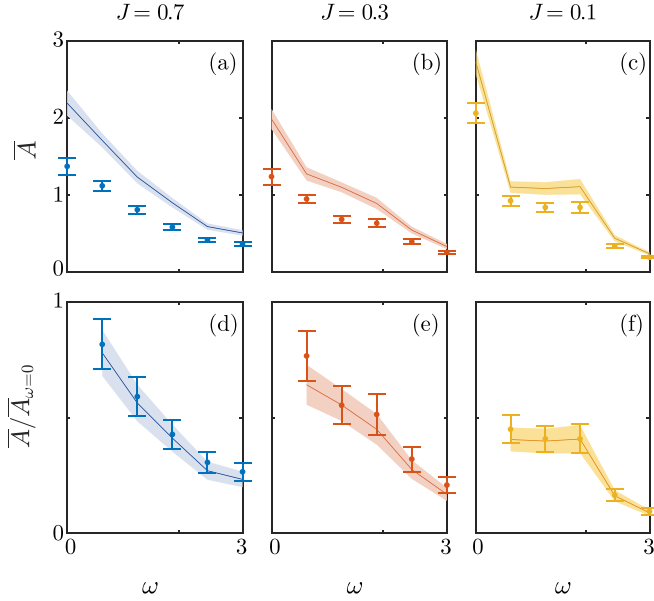


FIG. 3. (a)–(c) The spectral function of  $\hat{\sigma}_i^z$  averaged over position and 24 disorder realizations for different values of  $J$  (with  $w = 1$ ) for a three-site system. Lines show simulation results and circles show experimental results. (d)–(f) The spectral function normalized by its value at  $\omega = 0$ . At  $J = 0.7$ , the spectral response increases as  $\omega$  decreases while at  $J = 0.1$ , the spectrum is damped at low frequencies. The bands on the simulation curves and error bars on the experimental data signify the uncertainty after averaging over different disorder realizations. The points at  $\omega = 0$  in the top row are discontinuous with the rest of the curves since they arise from the diagonal elements of the observable in the eigenstate basis which have qualitatively different behavior than the off-diagonal ones.

circuits with the same structure can be well approximated by a depolarizing error model, whatever the origin of the noise [22]. Therefore, the mean density matrix after the application of the unitaries  $\{\hat{U}_H\}$  in Eq. (6) to an initial state  $|\Psi_0\rangle$  is

$$\bar{\rho} = \epsilon_m \overline{\hat{U}_H |\Psi_0\rangle \langle \Psi_0| \hat{U}_H^\dagger} + (1 - \epsilon_m) \frac{I}{D}, \quad (7)$$

where  $I$  is the identity matrix and  $D = 2^n$ ;  $\epsilon_m = p^m$ , where  $p$  is the disorder-averaged depolarization fidelity per Trotter step. The expectation value of  $\hat{a}$  at time  $t$  is

$$\overline{\langle \hat{a} \rangle(t)} = \text{Tr}(\bar{\rho}(t)\hat{a}) = p^m \overline{\text{Tr}(\hat{U}_H(t)|\Psi_0\rangle \langle \Psi_0| \hat{U}_H^\dagger(t)\hat{a})}. \quad (8)$$

Since the same number of Trotter steps  $m$  is used for measuring at all times, the corresponding spectrum obtained by Fourier transform becomes

$$\bar{A}(\omega) = p^m \int \overline{\text{Tr}(\hat{U}_H(t)|\Psi_0\rangle \langle \Psi_0| \hat{U}_H^\dagger(t)\hat{a}) e^{-i\omega t}} dt. \quad (9)$$

If we now divide by the zero-frequency component,

$$\frac{\bar{A}(\omega)}{\bar{A}(0)} = \frac{\int \overline{\text{Tr}(\hat{U}_H(t)|\Psi_0\rangle \langle \Psi_0| \hat{U}_H^\dagger(t)\hat{a}) e^{-i\omega t}} dt}{\int \overline{\text{Tr}(\hat{U}_H(t)|\Psi_0\rangle \langle \Psi_0| \hat{U}_H^\dagger(t)\hat{a})} dt}, \quad (10)$$

$p^m$  is canceled. We should thus essentially get a noiseless signal after the normalization. Figs. 3(d)–3(f) shows the normalized spectra. We see that the data match the normalized curves within the statistical uncertainty, especially at  $J = 0.1$

and  $J = 0.7$  which are deep in the localized and thermalized phase, respectively. Note that the estimated fidelity of the quantum computation obtained by multiplying the fidelities of the individual gates is only 54%, making the experimental reproduction of the theoretical curves in Fig. 3(b) remarkable.

From Eq. (7), it can be seen that the number of shots will need to increase as  $p^m$  in order to get a good number of samples from the first term. Since  $\hat{a}$  is a local operator, measuring it only involves a reduced density matrix of finite size, and therefore the error is independent of  $n$  when  $n$  is large enough. Therefore the number of shots depends exponentially on the number of Trotter steps but is independent of the number of qubits. Further, the coefficient of the exponential increase will be extremely small for the coming generation of trapped ion quantum computers, making system sizes large enough to show interesting dynamical effects accessible on quantum computers with no, or limited, error correction.

In Appendix B, we show simulation results for a system of seven spins. We see that the response at low frequencies is suppressed as the disorder increases, though it may still be larger than that at high frequencies. We thus believe that “suppression of the low-frequency response with increasing disorder” is a more accurate way of understanding the “zero-energy gap” than has been presented in the literature so far.

We next test the discreteness of the distribution by studying the linewidths  $\Gamma$  of the peaks in the spectrum. We expect the peaks in the localized phase to be narrower than in the thermalized phase on average. As shown in the Appendix of Ref. [18], the distribution should be skewed to larger linewidths, indicating the presence of resonant clusters of spins.

We use the following procedure to obtain the probability distribution of the linewidths.

- (1) Fit individual spectra (such as those in Fig. 2) with an interpolating polynomial and find the peaks.
- (2) For each peak, find the width corresponding to half the prominence of the peak.
- (3) Plot a normalized histogram corresponding to the probability distribution of the linewidths thus obtained.

The probability distributions  $P(\Gamma)$  are shown in Fig. 4 for different values of  $J$ . As expected, they are skewed to the right. In the inset of Fig. 4, we show that both the average linewidth as well as the skewness, which measures the probability of resonant clusters, are smaller at  $J = 0.1$  than at larger values of  $J$ . See Appendix C for a more detailed picture of how the spectrum changes with  $J$ .

In conclusion, we have presented a study of spectral functions of local operators that carry noise-resilient signatures of localization on a quantum computer. Since spectral functions determine transport properties, we anticipate that this algorithm along with the corresponding error mitigation technique will be useful in materials design applications of quantum computers.

Our error mitigation has worked so well that we foresee that the circuits run here could be extended to many more qubits and gates without a significant loss in the quality of the results. We hope to show this in future work. In particular, it is promising that the error mitigation used here did not require any extra data from the quantum computer. We encourage researchers to develop similarly scalable and noise-resistant

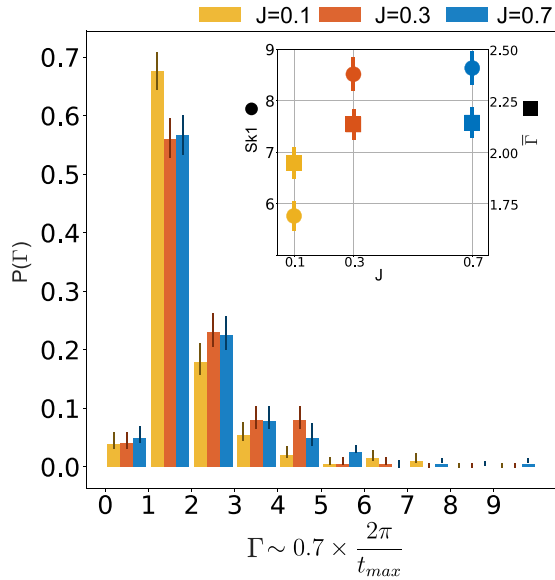


FIG. 4. The distribution histogram of linewidths  $\Gamma$  calculated as described in the text at different values of  $J$  from data taken on three qubits for 24 realizations. The bins are  $[0-1]$ ,  $[1-2]$ ,  $\dots$ , etc. The number of peaks used to generate the distribution is  $\sim 200$  for each value of  $J$ . We derive the errorbars shown in the plot by assuming each bin approximately follows a binomial distribution. The inset shows the Pearson's first coefficient of skewness,  $Sk1$ , and the average linewidth  $\bar{\Gamma}$ .

techniques for studying other unsolved problems in condensed matter physics on quantum computers.

#### ACKNOWLEDGMENTS

This work was supported by the ARO with funds from the Intelligence Advanced Research Projects Activity (IARPA) LogiQ program (Grant No. W911NF16-1-0082), the Army Research Office (ARO) MURI program on Modular Quantum Circuits (Grant No. W911NF1610349), the AFOSR MURI program on Optimal Quantum Measurements (Grant No. 5710003628), the NSF STAQ Practical Fully-Connected Quantum Computer Project, and the DOE BES Quantum Computing Program (Grant No. de-sc0019449). C.H.A. acknowledges financial support from CONACYT doctoral Grant No. 455378. N.M.L. acknowledges financial support by the NSF via the PFC@JQI, Grant No. PHY-1430094.

#### APPENDIX A: EXPERIMENTAL DETAILS

The system is based on a chain of  $^{171}\text{Yb}^+$  ions held in an RF Paul trap [23]. Each ion provides one physical qubit in the form of a pair of states in the hyperfine-split  $^2S_{1/2}$  ground level with an energy difference of 12.642821 GHz, which is insensitive to magnetic field fluctuations to first order. The qubits are initialized to  $|0\rangle$  by optical pumping and read out by state-dependent fluorescence detection [24]. Gates are realized by a pair of Raman beams derived from a single 355-nm mode-locked laser. These optical controllers consist of a global beam that illuminates the entire chain and an array of individual addressing beams. Single-qubit rotations

around the  $z$  axis are achieved by phase advances on the classical control signals. Single-qubit rotations around axes in the XY plane are realized by driving resonant Rabi rotations of defined phase, duration, and amplitude. Two-qubit gates are achieved by illuminating two selected ions with beat-note frequencies near the motional sidebands creating an effective Ising spin-spin interaction via transient entanglement between the two qubits and the motion in the trap [25–27]. Our scheme involves multiple modes of motion, which are disentangled from the qubits at the end of a two-qubit gate operation via an amplitude modulation scheme [28]. The effect of this scheme can be described by the unitary  $\exp(i\hat{\sigma}_i^x \hat{\sigma}_j^x \chi)$ , where  $\hat{\sigma}_i^x$  stands for the Pauli X operator of qubit  $i$ , and  $\chi$  stands for the rotation angle (gate angle). This type of gates are known as XX or Ising gate. Typical single- and two-qubit gate fidelities are 99.5(2)% and 98%–99%, respectively. The latter is limited by residual entanglement of the qubit states and the motional state of the ions due to intensity noise, and motional heating. The execution time of circuits implemented in this study is several milliseconds, which is much shorter than the qubit coherence time of our system (0.5 s).

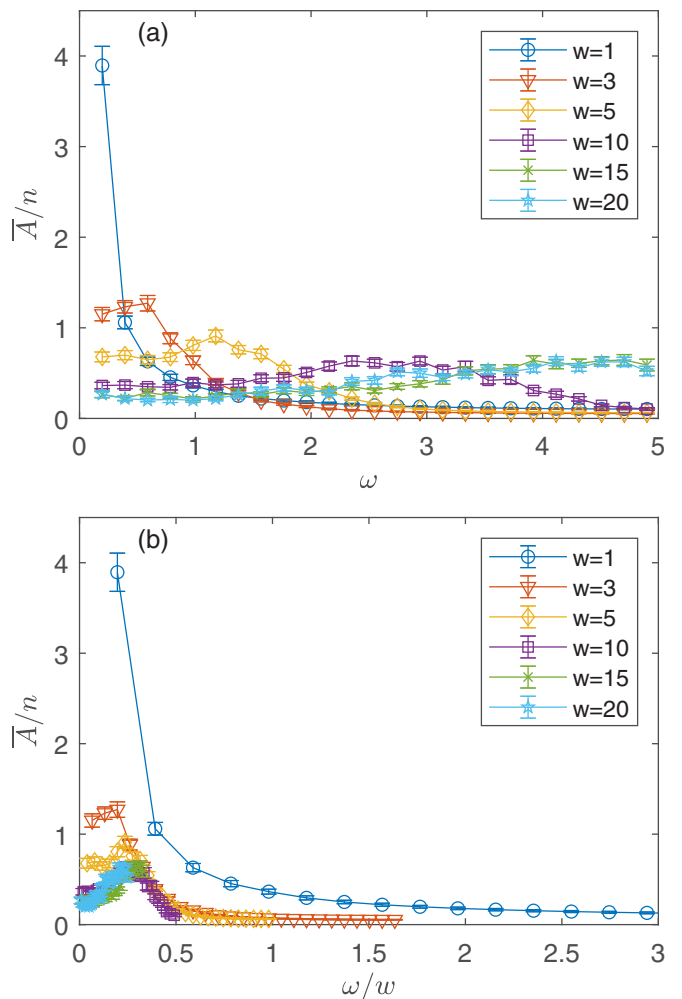


FIG. 5. (a) The simulated spectrum for  $n = 7$  spins averaged over 100 disorder configurations for fixed  $J = 1$ , while  $w$  is varied. (b) The same plot with the frequency scaled by  $w$ .

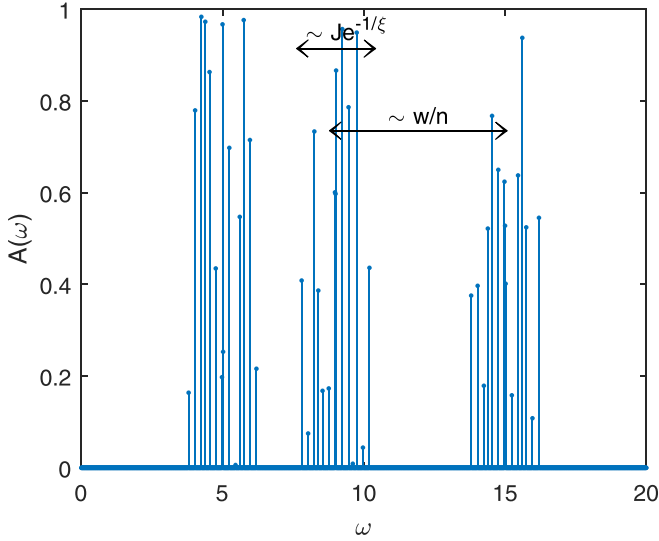


FIG. 6. A schematic example of the splitting of spectral lines according to the theoretical model in [20] for a localized system in the limit  $J \ll w$ .

Because of a slow drift in the laser alignment, the individual and two-qubit rotation angles change over time. We compensate for this by running an automated recalibration routine approximately every 20 min, which is the time needed to execute three circuits with 2400 repetitions each.

#### APPENDIX B: SIMULATION FOR LARGER SYSTEM SIZES

Figure 5(a) shows simulations for a seven-spin system for which  $J = 1$  and  $w$  is varied using 500 Trotter steps for each sample time and averaging over 100 disorder realizations. As  $w$  increases, the maximum of the spectrum shifts right while its magnitude at low frequencies goes down. The high-frequency regime represents one-body physics for which the energy scale is set by  $w$ . Therefore, in Fig. 5(b) which shows the same spectra on a plot where the frequency  $\omega$  has been scaled by the disorder magnitude  $w$ , the curves now lie on top of each other at high frequencies. Note that this plot is equivalent to fixing  $w = 1$  while varying  $J$ , and plotting the spectrum versus  $\omega$  as is done for the data in Fig. 3 of the paper. At low frequencies, there is a suppression of the spectral function as the ratio  $w/J$  increases, consistent

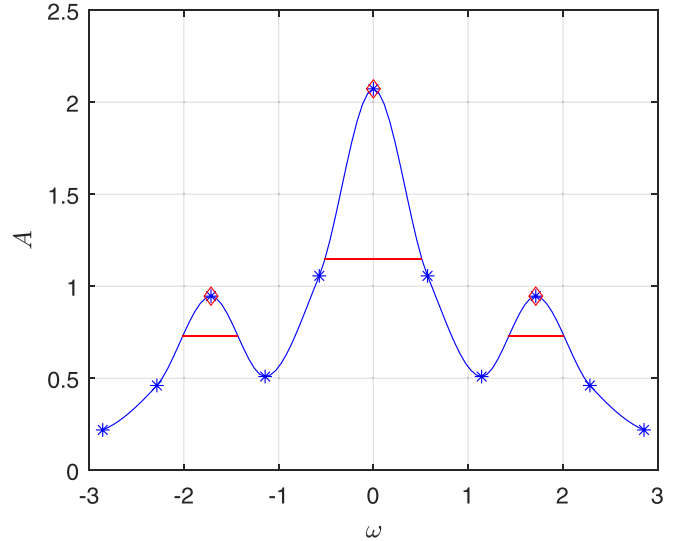


FIG. 7. An example of how the linewidths are extracted. The blue stars correspond to experimental data. The blue line consists of a polynomial fit. The red diamonds mark the peaks and the red horizontal lines mark the widths of the peaks.

with the results presented in the main text for a three-spin system.

#### APPENDIX C: LINEWIDTHS

When  $J = 0$ , the spectrum consists of  $n$  delta functions at  $\omega = \pm 2w\sqrt{h_i^{x^2} + h_i^{z^2}}$ . When the interaction  $J$  is turned on, each  $\delta$  function branches into a treelike structure. The splitting at each branch of the tree is proportional to  $J \exp(-d/\xi)$ , where  $d$  is the depth of the branch and  $\xi$  is the localization length [20]. Figure 6 shows a schematic example of this. When  $J$  is large enough, no discrete structure will remain and the spectrum will be continuous, indicating a transition to thermalization. In our experiment, we do not sample at enough points in the time evolution to resolve the hierarchical structure of the energy gaps but we can measure the total broadening of the original spectral line. The results for this are presented in Fig. 4 of the main text.

The linewidth extraction can be seen in Fig. 7. We use a piecewise cubic polynomial interpolation in MATLAB to fit the experimental data and then use the “findpeaks” function in MATLAB to find local maxima and their width at half the prominence of the peak.

- 
- [1] D. A. Abanin, E. Altman, I. Bloch, and M. Serbyn, *Rev. Mod. Phys.* **91**, 021001 (2019).
  - [2] R. Nandkishore and D. A. Huse, *Annu. Rev. Condens. Matter Phys.* **6**, 15 (2015).
  - [3] F. Alet and N. Laflorencie, *C. R. Phys.* **19**, 498 (2018).
  - [4] T. B. Wahl, A. Pal, and S. H. Simon, *Phys. Rev. X* **7**, 021018 (2017).
  - [5] A. Chandran, J. Carrasquilla, I. H. Kim, D. A. Abanin, and G. Vidal, *Phys. Rev. B* **92**, 024201 (2015).
  - [6] A. M. Childs, D. Maslov, Y. Nam, N. J. Ross, and Y. Su, *Proc. Natl. Acad. Sci.* **115**, 9456 (2018).
  - [7] H. P. Lüschen, P. Bordia, S. Scherg, F. Alet, E. Altman, U. Schneider, and I. Bloch, *Phys. Rev. Lett.* **119**, 260401 (2017).
  - [8] H. P. Lüschen, P. Bordia, S. S. Hodgman, M. Schreiber, S. Sarkar, A. J. Daley, M. H. Fischer, E. Altman, I. Bloch, and U. Schneider, *Phys. Rev. X* **7**, 011034 (2017).
  - [9] P. Bordia, H. Lüschen, S. Scherg, S. Gopalakrishnan, M. Knap, U. Schneider, and I. Bloch, *Phys. Rev. X* **7**, 041047 (2017).

- [10] P. Bordia, H. P. Lüschen, S. S. Hodgman, M. Schreiber, I. Bloch, and U. Schneider, *Phys. Rev. Lett.* **116**, 140401 (2016).
- [11] A. Rubio-Abadal, J.-y. Choi, J. Zeiher, S. Hollerith, J. Rui, I. Bloch, and C. Gross, *Phys. Rev. X* **9**, 041014 (2019).
- [12] T. Kohlert, S. Scherg, X. Li, H. P. Lüschen, S. Das Sarma, I. Bloch, and M. Aidelsburger, *Phys. Rev. Lett.* **122**, 170403 (2019).
- [13] J. Smith, A. Lee, P. Richerme, B. Neyenhuis, P. W. Hess, P. Hauke, M. Heyl, D. A. Huse, and C. Monroe, *Nat. Phys.* **12**, 907 (2016).
- [14] P. Hess, P. Becker, H. Kaplan, A. Kyprianidis, A. Lee, B. Neyenhuis, G. Pagano, P. Richerme, C. Senko, J. Smith *et al.*, *Philos. Trans. R. Soc. A* **375**, 20170107 (2017).
- [15] P. Roushan, C. Neill, J. Tangpanitanon, V. M. Bastidas, A. Megrant, R. Barends, Y. Chen, Z. Chen, B. Chiaro, A. Dunsworth, A. Fowler, B. Foxen, M. Giustina, E. Jeffrey, J. Kelly, E. Lucero, J. Mutus, M. Neeley, C. Quintana, D. Sank, A. Vainsencher, J. Wenner, T. White, H. Neven, D. G. Angelakis, and J. Martinis, *Science* **358**, 1175 (2017).
- [16] B. Chiaro, C. Neill, A. Bohrdt, M. Filippone, F. Arute, K. Arya, R. Babbush, D. Bacon, J. Bardin, R. Barends, S. Boixo, D. Buell, B. Burkett, Y. Chen, Z. Chen, R. Collins, A. Dunsworth, E. Farhi, A. Fowler, B. Foxen, C. Gidney, M. Giustina, M. Harrigan, T. Huang, S. Isakov, E. Jeffrey, Z. Jiang, D. Kafri, K. Kechedzhi, J. Kelly, P. Klimov, A. Korotkov, F. Kostritsa, D. Landhuis, E. Lucero, J. McClean, X. Mi, A. Megrant, M. Mohseni, J. Mutus, M. McEwen, O. Naaman, M. Neeley, M. Niu, A. Petukhov, C. Quintana, N. Rubin, D. Sank, K. Satzinger, A. Vainsencher, T. White, Z. Yao, P. Yeh, A. Zalcman, V. Smelyanskiy, H. Neven, S. Gopalakrishnan, D. Abanin, M. Knap, J. Martinis, and P. Roushan, [arXiv:1910.06024v2](https://arxiv.org/abs/1910.06024v2).
- [17] X. Zou, S. P. Premaratne, M. A. Rol, S. Johri, V. Ostroukh, D. J. Michalak, R. Caudillo, J. S. Clarke, L. DiCarlo, and A. Y. Matsuura, *IEEE Trans. Quantum Eng.* **1**, 1 (2020).
- [18] S. Johri, R. Nandkishore, and R. N. Bhatt, *Phys. Rev. Lett.* **114**, 117401 (2015).
- [19] S. D. Geraedts, N. Regnault, and R. M. Nandkishore, *New J. Phys.* **19**, 113021 (2017).
- [20] R. Nandkishore, S. Gopalakrishnan, and D. A. Huse, *Phys. Rev. B* **90**, 064203 (2014).
- [21] N. M. Linke, S. Johri, C. Figgatt, K. A. Landsman, A. Y. Matsuura, and C. Monroe, *Phys. Rev. A* **98**, 052334 (2018).
- [22] F. Arute, K. Arya, R. Babbush, D. Bacon, J. C. Bardin, R. Barends, R. Biswas, S. Boixo, F. G. S. L. Brandao, D. A. Buell, B. Burkett, Y. Chen, Z. Chen, B. Chiaro, R. Collins, W. Courtney, A. Dunsworth, E. Farhi, B. Foxen, A. Fowler, C. Gidney, M. Giustina, R. Graff, K. Guerin, S. Habegger, M. P. Harrigan, M. J. Hartmann, A. Ho, M. Hoffmann, T. Huang, T. S. Humble, S. V. Isakov, E. Jeffrey, Z. Jiang, D. Kafri, K. Kechedzhi, J. Kelly, P. V. Klimov, S. Knysh, A. Korotkov, F. Kostritsa, D. Landhuis, M. Lindmark, E. Lucero, D. Lyakh, S. Mandra, J. R. McClean, M. McEwen, A. Megrant, X. Mi, K. Michielsen, M. Mohseni, J. Mutus, O. Naaman, M. Neeley, C. Neill, M. Y. Niu, E. Ostby, A. Petukhov, J. C. Platt, C. Quintana, E. G. Rieffel, P. Roushan, N. C. Rubin, D. Sank, K. J. Satzinger, V. Smelyanskiy, K. J. Sung, M. D. Trevithick, A. Vainsencher, B. Villalonga, T. White, Z. J. Yao, P. Yeh, A. Zalcman, H. Neven, and J. M. Martinis, *Nature (London)* **574**, 505 (2019).
- [23] S. Debnath, N. M. Linke, C. Figgatt, K. A. Landsman, K. Wright, and C. Monroe, *Nature (London)* **536**, 63 (2016).
- [24] S. Olmschenk, K. C. Younge, D. L. Moehring, D. N. Matsukevich, P. Maunz, and C. Monroe, *Phys. Rev. A* **76**, 052314 (2007).
- [25] K. Mølmer and A. Sørensen, *Phys. Rev. Lett.* **82**, 1835 (1999).
- [26] E. Solano, R. L. de Matos Filho, and N. Zagury, *Phys. Rev. A* **59**, R2539(R) (1999).
- [27] G. Milburn, S. Schneider, and D. James, *Fortschr. Phys.* **48**, 801 (2000).
- [28] T. Choi, S. Debnath, T. A. Manning, C. Figgatt, Z.-X. Gong, L.-M. Duan, and C. Monroe, *Phys. Rev. Lett.* **112**, 190502 (2014).